Croatian Society for Materials Protection

Metalurgija/Metallurgy

Vol. 66 No. 2 / 2027

Die-Forging Process Design and Forming-Load Optimization for a G55 Wheel-Hub-Bearing Inner Ring

J. H. Huang [1*], B. Zhang [1], Z. L. Liao [1], H. B. Fu [2], and H. P. Ma [1]

https://doi.org/10.64486/m.66.2.6

[1] School of Intelligent Manufacturing and Energy Engineering, Zhejiang University of Science & Technology, Hangzhou 310023, China
[2] Zhejiang Zhaofeng Mechanical and Electronic Co., Ltd., Hangzhou 311231, China
* Correspondence: huangjianghua@zust.edu.cn

Type of the Paper: Article
Received: August 26, 2025
Accepted: August 19, 2026

Abstract: This study characterized the hot-deformation behavior of G55 steel used in wheel-hub-bearing inner rings and obtained true stress-strain curves from compression tests. A three-stage die-forging route, comprising upsetting, pre-forging, and final forging, was simulated in DEFORM-3D. An $L_9(3^3)$ orthogonal design with a smaller-the-better signal-to-noise (S/N) analysis was used to reduce the maximum forming load. The influence of the investigated factors decreased in the order initial billet temperature, shear-friction factor, and upper-die velocity. The lowest simulated load was 1.29×10^7 N at 1200 °C, a friction factor of 0.3, and an upper-die velocity of 100 mm·s^{-1}. Trial forgings produced under these conditions were fully filled and showed no visible surface defects. The optimized process therefore provides a feasible process window for manufacturing the investigated inner ring.

Keywords: G55 steel; wheel-hub-bearing inner ring; die forging; finite-element simulation; orthogonal design; forming load

1. Introduction

G55 steel is a medium-carbon bearing steel that combines high tensile strength, wear resistance, and impact resistance for components subjected to heavy loads. Vrček et al. characterized the micropitting and wear resistance of G55 bearing steel [1]. Sun et al. examined the effect of residual-temperature normalizing on the properties of G55 wheel-hub-bearing forgings [2]. Wheel-hub-bearing units support the wheel and vehicle body while sustaining complex service loads [3]–[5]. The inner ring contains circumferentially distributed features and a flange connected by several curved surfaces, as shown in Figure 1. This complex geometry makes reducing the forming load essential for limiting die stresses and extending die service life.

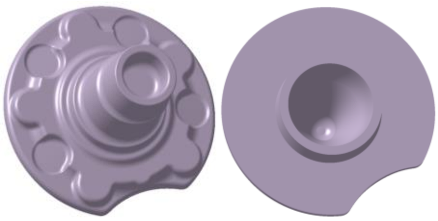

Figure 1. Three-dimensional model of the automotive wheel-hub-bearing inner ring

Forging parameters directly influence surface quality, cavity filling, and die service life. Liu et al. optimized an outer-ring die and reported improvements in forging quality and die life [6]. Ji et al. evaluated process parameters for wheel-hub-bearing forgings and obtained parts that met product requirements [7]. Other studies also show that process parameters affect metal flow, forming quality, and die loading [8]–[10]. Li et al. optimized finite-element parameters for hub-bearing-ring forging by considering the effects of friction, temperature, and velocity on forming load and die wear [11]. Hawryluk et al. showed that non-uniform temperature fields can impair forging quality and accelerate die wear through localized overheating [12]. Samal reported that process parameters strongly influence forging geometry and microstructural evolution during closed-die hot forging [13].

In this study, true stress-strain curves were first obtained from single-pass compression tests at different temperatures and strain rates. A coupled three-dimensional finite-element model was then used to simulate upsetting, pre-forging, and final forging. An orthogonal design was applied to rank three process factors and identify the combination that minimized the maximum forming load. Finally, trial forgings and metallographic observations were used to evaluate cavity filling, visible surface defects, and the resulting microstructure.

2. Materials and methods

2.1 Hot-deformation behavior of G55 steel

True stress-strain curves were obtained to characterize the hot-deformation behavior of G55 steel. Cylindrical specimens with a diameter of 8 mm and a height of 12 mm were compressed in a single pass to a 50 % height reduction. The tests were conducted under the temperature and strain-rate conditions listed in Table 1. The resulting data were imported into the DEFORM-3D material library for subsequent finite-element simulations. Table 2 lists the chemical composition of G55 steel.

Table 1. Isothermal compression-test parameters

Deformation temperature (°C)	**Strain rate / s^{-1}**
900, 1000, 1100, 1200	0.01
	0.1
	1
	10

Table 2. Chemical composition of G55 steel / wt. %

C	**Si**	**Mn**	**P**	**S**	**Cu**	**Al**
0.52–0.60	≤0.40	0.60–0.90	≤0.025	≤0.015	≤0.30	≤0.05

The true stress-strain curves in Figure 2 show that the hot-deformation response of G55 steel was sensitive to both temperature and strain rate. At 0.01 and 0.1 s^{-1}, the curves exhibited pronounced dynamic-recrystallization characteristics [14]–[15]. At strain rates of 1 s^{-1} or higher, dynamic recrystallization was increasingly suppressed, whereas work hardening increased the deformation resistance [16]–[18]. Consequently, the highest flow stress occurred at 10 s^{-1}.

https://doi.org/10.64486/m.66.2.6

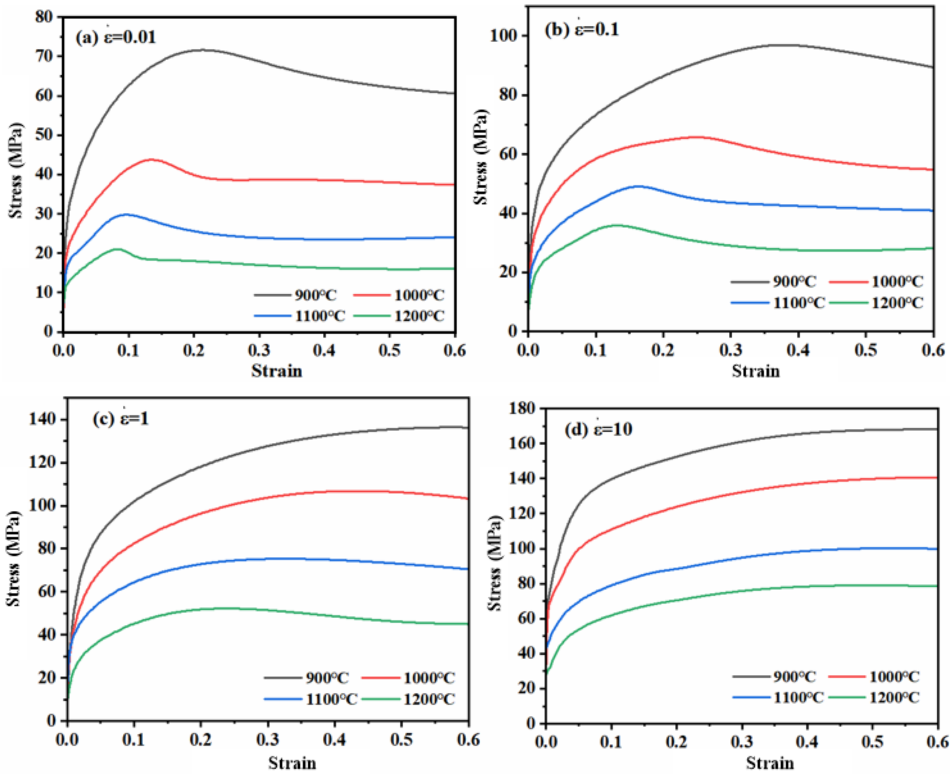

Figure 2. True stress-strain curves of G55 steel under different deformation conditions

2.2 Finite-element modeling

A three-dimensional, thermomechanically coupled finite-element model was developed in DEFORM-3D for upsetting, pre-forging, and final forging. The billet and die geometries were created in CATIA and imported into DEFORM-3D as STL files. The upsetting billet was a G55 steel cylinder with a diameter of 60 mm and a height of 128.7 mm. Because the geometry and loading were symmetric about a longitudinal plane through the central axis, one half of the assembly was modeled. A symmetry boundary condition was applied on this plane to reduce the computational cost.

The billet was modeled as an elastoplastic deformable body using the experimentally measured true stress-strain data described in Section 2.1. After each stage, the deformed billet geometry was imported directly into the next simulation. The temperature, strain, and strain-rate fields were also inherited to represent the accumulated thermomechanical history of the three-stage process.

Under the reference condition, the billet entered upsetting at 1200 °C, whereas the dies and surrounding environment were initialized at 20 °C. The upper die moved downward at a constant velocity of 100 $mm\cdot s^{-1}$. Die-billet contact was described using a shear-friction model with a reference friction factor of 0.3. Environmental heat exchange was neglected, and die-billet heat transfer was activated only during the final-forging stage. The billet mesh contained approximately 120,000 elements in each forging stage.

The minimum element sizes were 0.776 mm, 0.639 mm, and 0.699 mm for upsetting, pre-forging, and final forging, respectively. All dies were treated as rigid during upsetting and pre-forging. In the final-forging model, the lower die was modeled as an elastic body with approximately 110,000 elements. The lower die used AISI H13 tool-steel properties from the DEFORM-3D material database, and its supporting surface was fully constrained.

The upper-die displacement increment was 0.26 mm per simulation step. The upsetting, pre-forging, and final-forging simulations comprised 185 steps, 296 steps, and 300 steps, respectively. These settings corresponded to nominal displacements of 48.10 mm, 76.96 mm, and 78.00 mm. Each simulation was terminated after the prescribed number of steps, when the billet reached the required deformation state.

https://doi.org/10.64486/m.66.2.6

Figures 3–5 show the finite-element models for upsetting, pre-forging, and final forging. Model preparation included geometry import, material assignment, meshing, contact definition, and die-motion settings.

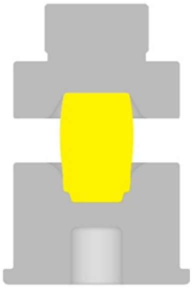

Figure 3. Upsetting finite-element model

Figure 4. Pre-forging finite-element model

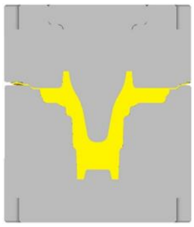

Figure 5. Final-forging finite-element model

Figure 6 shows the deformation sequence during upsetting. As deformation progressed, the die cavity restricted metal flow near the billet base. Continued downward motion of the upper die compressed the billet core and promoted radial expansion.

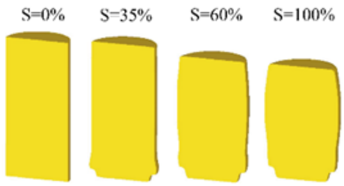

Figure 6. Deformation sequence during upsetting

Figure 7 shows the deformation sequence during pre-forging. Axial compression first drove radial flow and initiated the upper hole. Complex multidirectional flow then filled the die cavity progressively. As the upper-die stroke increased, the cavity became nearly full and the lower hole began to form.

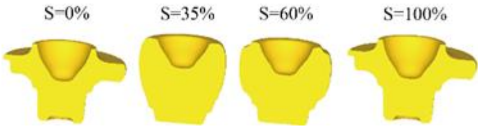

Figure 7. Deformation sequence during pre-forging

Figure 8 shows the deformation sequence during final forging. The upper hole formed first and deepened progressively, followed by the upper end face. The lower hole formed during the final stage.

Figure 8. Deformation sequence during final forging

2.3 Process-parameter optimization by orthogonal design

Maximum forming load governs both the required press capacity and the mechanical loading of the forging dies. It was therefore selected as the optimization response. Three controllable factors were considered: initial billet temperature (A), shear-friction factor (B), and upper-die velocity (C). Each factor was evaluated at three levels within the investigated process window. An $L_9(3^3)$ orthogonal array was used to evaluate factor effects

https://doi.org/10.64486/m.66.2.6

with nine simulations [19]–[22]. Table 3 lists the factor levels, and Table 4 presents the simulated maximum forming loads.

Table 3. Factors and levels used in the orthogonal design

Level	A: Initial billet temperature / °C	B: Shear-friction factor	C: Upper-die velocity / mm • s^{-1}
1	1200	0.4	75
2	1150	0.3	100
3	1100	0.2	125

Table 4. $L_9(3^3)$ orthogonal array and simulated maximum forming loads

Trial no.	A:Initial billet temperature / °C	B:Shear-friction factor	C:Upper-die velocity mm • s^{-1}	Maximum forming load 10^7 N
1	1200	0.4	75	1.69
2	1200	0.3	100	1.29
3	1200	0.2	125	1.60
4	1150	0.4	100	2.15
5	1150	0.3	125	2.00
6	1150	0.2	75	1.74
7	1100	0.4	125	2.53
8	1100	0.3	75	2.21
9	1100	0.2	100	2.27

Because the objective was to minimize forming load, the smaller-the-better signal-to-noise (S/N) ratio was used to evaluate the simulation results:

$$\eta = -10\log_{10}\left(\frac{1}{n}\sum_{i=1}^{n} y_i^2\right) \quad (1)$$

where η is the S/N ratio, y_i is the forming-load response, and n is the number of observations in each numerical trial. Each trial produced a single forming-load value; therefore, n = 1. A larger S/N ratio, corresponding to a less negative value, indicates a lower forming load. The mean S/N ratio at each level was calculated for factors A–C, and the factor effect was evaluated using the range R:

$$R_j = max(\bar{\eta}_{jk}) - min(\bar{\eta}_{jk}) \quad (2)$$

where $\bar{\eta}_{jk}$ denotes the mean S/N ratio of factor j at level k. A larger R indicates a stronger effect of the corresponding factor on the forming load.

Table 5. Response table for the mean forming-load S/N ratios / dB

Level	A: Initial billet temperature	B: Shear-friction factor	C: Upper-die velocity
1	-3.62	-6.42	-5.42
2	-5.82	-5.04	-5.32
3	-7.36	-5.34	-6.06
Range R	3.74	1.38	0.74
Rank	1	2	3

https://doi.org/10.64486/m.66.2.6

Table 5 shows that initial billet temperature had the largest S/N-ratio range (R = 3.74 dB). The ranges for shear-friction factor and upper-die velocity were 1.38 and 0.74 dB, respectively. The factors were therefore ranked A > B > C. The highest mean S/N ratios for A, B, and C occurred at levels 1, 2, and 2, respectively. The predicted optimum was A1B2C2, corresponding to 1200 °C, a friction factor of 0.3, and an upper-die velocity of 100 mm • s^{-1} .

Combination A1B2C2 corresponded to trial 2 in Table 4 and produced a maximum forming load of 1.29 × 10^7 N. This was the lowest value among the nine simulations and supported the selection from the S/N-ratio analysis. However, trial 2 belonged to the original orthogonal array and was not an independent confirmation test.

3. Experimental verification

Figure 9 shows wheel-hub-bearing inner rings produced by hot-die forging under the selected process conditions. The forgings were fully filled and had smooth, flat surfaces. No visible cracks, folds, or other macroscopic forming defects were observed.

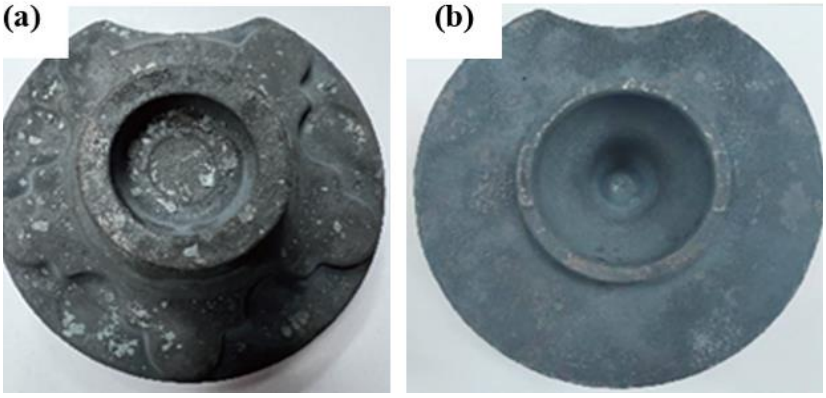

Figure 9. Wheel-hub-bearing inner-ring forgings produced under the optimized process conditions

The final forgings were sectioned for metallographic examination. Figure 10 shows a fine and relatively uniform distribution of ferrite and pearlite, with no observed martensite or bainite. This ferrite–pearlite microstructure is consistent with the intended condition of the forged component.

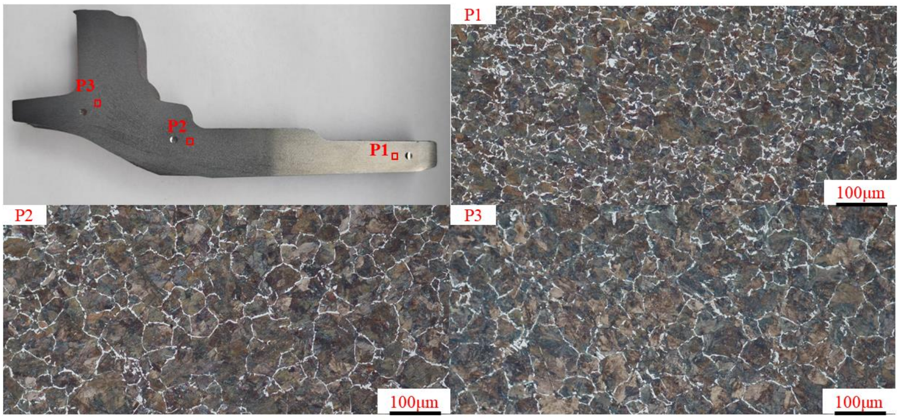

Figure 10. Microstructure of the final forging

https://doi.org/10.64486/m.66.2.6

4. Discussion

The orthogonal analysis identified initial billet temperature as the dominant factor controlling the maximum forming load. Its mean S/N-ratio range was 3.74 dB, compared with 1.38 dB for friction and 0.74 dB for die velocity. The selected A1B2C2 condition produced the lowest simulated maximum load, 1.29×10^7 N. This ranking is consistent with the study by Jantepa et al. [22] on AISI 1045 ball-joint forging. They attributed 62.30 % and 59.50 % of the preforming and finishing force variation, respectively, to billet temperature, with friction ranking second. Li et al. [11] similarly considered billet temperature, friction, die temperature, and die speed when optimizing hub-bearing-ring forging load and die wear.

The dominant temperature effect arises from the strong temperature dependence of G55 flow stress. At a fixed strain rate, the compression curves in Figure 2 show that flow stress decreased as deformation temperature increased. A higher initial temperature therefore reduced plastic-deformation resistance through thermally activated dislocation motion and dynamic softening. This reduction lowered the force required to fill the die cavity. Hawryluk et al. [12] similarly emphasized the need to control billet and tool temperature distributions in industrial hot forging. However, 1200 °C was the upper limit investigated here. This result identifies the best temperature among the tested levels and should not be extrapolated beyond the studied range. At higher temperatures, oxidation, grain growth, and excessive die heating may offset the load reduction.

The shear-friction factor ranked second because interfacial friction controls billet sliding and radial flow along the die surface. Higher friction restricts cavity filling and increases redundant shear deformation, thereby raising the pressure and load required for complete filling. Wang et al. [21] similarly found that increasing friction raised effective stress in warm forging, whereas improved lubrication reduced the forming force. In Table 5, however, the mean S/N ratio at 0.3 exceeded that at 0.2 only moderately. This non-monotonic difference does not establish that a friction factor of 0.3 is universally optimal. The $L_9(3^3)$ design included neither replicates nor interaction columns. Accordingly, the observed difference may partly reflect the temperature and velocity combinations assigned to those runs.

Upper-die velocity had the smallest effect because it influenced load through two competing mechanisms. Increasing velocity raised the strain rate and could increase G55 flow stress, as indicated by the compression curves. Conversely, a shorter forming time limited billet cooling and could maintain lower deformation resistance. The model neglected environmental heat exchange and activated die-billet heat transfer only during final forging. Consequently, the thermal-retention benefit of higher velocity was limited under the adopted assumptions. The intermediate optimum at 100 $mm \cdot s^{-1}$, followed by a poorer response at 125 $mm \cdot s^{-1}$, suggests stronger strain-rate hardening at the highest velocity. Wang et al. [21] instead observed decreasing effective force with increasing striking speed during warm forging of spiral bevel gears. This contrast shows that velocity effects depend on material behavior, geometry, thermal boundary conditions, and forming stage.

Trial forgings and metallographic observations support the feasibility of A1B2C2 for producing fully filled components without observed macroscopic defects. However, they do not quantitatively validate the predicted maximum load because no experimental load–displacement curve was recorded. Moreover, A1B2C2 was already included as trial 2, and each orthogonal-array condition yielded only one simulated response. Chen and Jung [20] used analysis of variance to evaluate parameter effects and variation in a robust forging design. By contrast, the present design cannot independently estimate numerical error, factor interactions, or response variability. The conclusions are therefore limited to the tested factor levels and to the adopted constant-friction and heat-transfer assumptions. Accordingly, the identified optimum should be regarded as valid only within the investigated design space and should be verified by an independent confirmation experiment. Future work will combine repeated, instrumented forging trials with calibrated friction and heat-transfer parameters. An expanded response-surface design will quantify factor interactions and extend the optimization to die life and microstructural uniformity.

https://doi.org/10.64486/m.66.2.6

5. Conclusions

(1) G55 flow stress increased with strain rate and decreased with deformation temperature under the investigated hot-compression conditions.

(2) A three-stage die-forging route comprising upsetting, pre-forging, and final forging was simulated in DEFORM-3D. The $L_9(3^3)$ orthogonal design ranked the factors as initial billet temperature > shear-friction factor > upper-die velocity. The lowest simulated maximum load was 1.29×10^7 N and occurred at 1200 °C, a friction factor of 0.3, and an upper-die velocity of 100 $mm \cdot s^{-1}$.

(3) Trial forgings produced under the selected condition were fully filled and showed no visible cracks, folds, or other macroscopic defects. Metallographic examination revealed a fine ferrite–pearlite microstructure without observed martensite or bainite. These findings support the selected process as a practical basis for manufacturing the investigated inner ring.

References

[1] A. Vrček, T. Hultqvist, T. Johannesson, P. Marklund, R. Larsson, Micro-pitting and wear characterization for different rolling bearing steels: Effect of hardness and heat treatments, *Wear* 458–459 (2020) 203404, https://doi.org/10.1016/j.wear.2020.203404

[2] C. Sun, G. Cao, H. Fu, F. Chen, J. Huang, H. Ji, Study on the influence of residual temperature normalizing process on the performance of automotive hub bearing forgings, *Journal of Materials Research and Technology* 39 (2025) 7792–7802, https://doi.org/10.1016/j.jmrt.2025.11.066

[3] L. Zhao, Q. Li, J. Z. Feng, S. Zheng, Service life prediction method for wheel-hub-bearing under random multi-axial wheel loading, *Engineering Failure Analysis* 122 (2021) 105211, https://doi.org/10.1016/j.engfailanal.2020.105211

[4] Y. Lee, S. Yu, K. Kang, S. Lee, Development of load spectrum for wheel hub bearings of a commercial vehicle through road load data acquisition, *International Journal of Automotive Technology* 27 (2026) 1, 379–390 (published online 25 July 2025), https://doi.org/10.1007/s12239-025-00311-y

[5] P. Cang, X. Zhang, W. Cui, Static and modal models of automotive wheel hubs based on lightweight design and cost-effectiveness, *Applied Sciences* 13 (2023) 18, 10164, https://doi.org/10.3390/app131810164

[6] P. Y. Liu, N. Z. Kang, J. H. Huang, et al., Optimization design and simulation analysis of forging process for automotive wheel hub bearing outer ring, *Forging & Stamping Technology* 50 (2025) 1, 8–19 (in Chinese), https://doi.org/10.13330/j.issn.1000-3940.2025.01.002

[7] H. C. Ji, R. Zhang, N. Z. Kang, J. H. Huang, Simulation analysis of wheel bearing forging process based on DEFORM, *Metalurgija* 64 (2025) 1–2, 87–90. [Online]. Available: https://hrcak.srce.hr/319869 (accessed 28 July 2026).

[8] C. L. Zhai, Y. L. Tang, Q. Q. Xu, X. X. Sun, J. Miao, Wear analysis and optimization of hot forging die for automotive torque arm based on orthogonal experiment, *Forging & Stamping Technology* 46 (2021) 5, 185–189 (in Chinese), https://doi.org/10.13330/j.issn.1000-3940.2021.05.029

[9] M. H. Zhang, S. M. Liu, C. Gao, et al., Optimization of hot forging process for wheel hub flange based on Taguchi method, *Forging & Stamping Technology* 42 (2017) 8, 17–21, (in Chinese), https://doi.org/10.13330/j.issn.1000-3940.2017.08.004

[10] J. Y. Xu, B. S. Sun, N. Li, Research on forging forming force in the composite technology of cross wedge rolling (CWR) and forging for universal joint fork, *Metalurgija* 58 (2019) 1–2, 131–134. [Online]. Available: https://hrcak.srce.hr/206516 (accessed 28 July 2026).

https://doi.org/10.64486/m.66.2.6

[11] J. Li, A. Wang, J. Lu, N. Kang, J. Huang, B. Wang, Q. Fan, Optimization of precision die forging process parameters of hub bearing ring based on response surface method, *Journal of Materials Engineering and Performance* 34 (2025) 18, 20570–20585, https://doi.org/10.1007/s11665-025-11161-1

[12] M. Hawryluk, Ł. Dudkiewicz, J. Krawczyk, M. Janik, M. Lachowicz, M. Skwarski, Challenges in temperature measurement in hot forging processes: Impact of measurement method selection on accuracy and errors in the context of tool life and forging quality, *Materials* 18 (2025) 16, 3850, https://doi.org/10.3390/ma18163850

[13] C. Samal, Study of process parameters towards improving efficiency of closed die hot forging process, M.Tech. thesis, National Institute of Technology Rourkela, India, 2014. [Online]. Available: https://core.ac.uk/download/pdf/53190286.pdf (accessed 28 July 2026).

[14] J. Sun, J. Li, Z. Huang, X. Zhang, D. Wang, S. Liu, Microstructure evolution and dynamic recrystallization of a low-density steel during isothermal compression, *Chinese Journal of Materials Research* 38 (2024) 10, 768–781 (in Chinese), https://doi.org/10.11901/1005.3093.2024.082

[15] Y. Pei, M. Yuan, E. Wei, M. Yu, B. Teng, Effect of strain rate on dynamic recrystallization mechanism of Mg-Gd-Y-Sm-Zr alloy during hot compression, *Journal of Materials Research and Technology* 25 (2023) 5038–5050, https://doi.org/10.1016/j.jmrt.2023.07.029

[16] S. Liu, D. Kent, H. Zhan, N. Doan, C. Wang, S. Yu, M. Dargusch, G. Wang, Influence of strain rate and crystallographic orientation on dynamic recrystallization of pure Zn during room-temperature compression, *Journal of Materials Science & Technology* 86 (2021) 237–250, https://doi.org/10.1016/j.jmst.2020.12.077

[17] Z. Li, J. Ge, B. Kong, D. Luo, Z. Wang, X. Zhang, Strain rate dependence and recrystallization modeling for TC18 alloy during post-deformation annealing, *Materials* 16 (2023) 3, 1140, https://doi.org/10.3390/ma16031140

[18] Y. Q. Zhang, G. Z. Quan, S. Lei, J. Zhao, W. Xiong, Description of dynamic recrystallization behaviors and grain evolution mechanisms during the hot forming process for SAE 5137H steel, *Materials* 15 (2022) 16, 5593, https://doi.org/10.3390/ma15165593

[19] G. Xie, S. Zhang, H. Li, L. Wang, W. Du, C. Zhao, H. Jia, A double-layer optimization method for forging process parameters of hinge beam structure and size of intermediate billet, *Journal of Mechanical Science and Technology* 37 (2023) 10, 5307–5319, https://doi.org/10.1007/s12206-023-0933-4

[20] X. Chen, D. Jung, Gear hot forging process robust design based on finite element method, *Journal of Mechanical Science and Technology* 22 (2008) 9, 1772–1778, https://doi.org/10.1007/s12206-008-0515-5

[21] Z. Wang, C. Jiang, B. Wei, Y. Wang, Numerical simulation and process parameter optimization of warm forging near-net forming for spiral bevel gear, *Applied Sciences* 14 (2024) 3, 1147, https://doi.org/10.3390/app14031147

[22] N. Jantepa, N. Siripath, S. Suranuntchai, Predictive modeling and optimization of hot forging parameters for AISI 1045 ball joints using Taguchi methodology and finite element analysis, *Metals* 14 (2024) 10, 1198, https://doi.org/10.3390/met14101198

https://doi.org/10.64486/m.66.2.6